Journal of Cluster Science
https://doi.org/10.1007/s10876-022-02373-9

ORIGINAL PAPER

Synthesis, Characterization and Potent Antibacterial Activity of Metal-Substituted Spinel Ferrite Nanoparticles

Shadab Dabagh[1] · Somayeh Asadi Haris[2] · Yavuz Nuri Ertas[1,3]

Received: 30 August 2022 / Accepted: 11 October 2022

Abstract

$CuFe_2O_4$, $ZnFe_2O_4$, and $MnFe_2O_4$ ferrite nanoparticles (NPs) have been synthesized through auto composition sol–gel method, and citric acid was used as the chelating agent. Phase analysis of nanoparticles confirmed the pure cubic spinel structure. The morphology and elemental composition verified the presence of all the elements in prepared samples and size distribution of NPs was estimated to be ~ 20–30 nm. Saturation magnetizations and magneton numbers were in the range of 53–67 emu/g and 2.29–3.12 n_B, respectively. $MnFe_2O_4$ NPs exhibited the strongest magnetization of all NPs. Highly significant antibacterial activity (22 mm zone of inhibition) of $CuFe_2O_4$ NPs was observed against Gram negative bacteria, *Escherichia coli.* The broth microdilution assay result demonstrated the lower minimum inhibitory concentration and minimum bactericidal concentration values for $CuFe_2O_4$ as well as for $ZnFe_2O_4$ and $MnFe_2O_4$ NPs in combination. Furthermore, the in vitro cytotoxicity assay revealed that NPs were not toxic to HSF 1184 cell lines at 400 µg/ml concentration, hence the prepared NPs are safe, affordable, sustainable composite and can be used for potent antibacterial applications.

Graphical Abstract

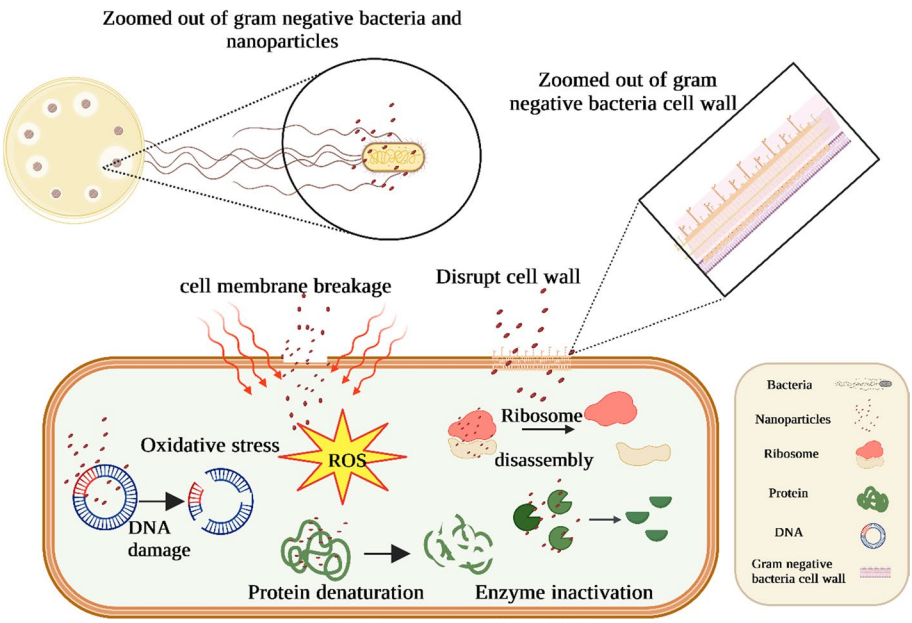

Keywords Spinel Ferrite · *Escherichia coli* · Antibacterial · Cytotoxicity · Nanoparticle

✉ Yavuz Nuri Ertas
yavuzertas@erciyes.edu.tr

Extended author information available on the last page of the article

Published online: 26 October 2022

Introduction

Ferrites, one of the most substantial magnetic materials, consist of two inverse and normal spinel structures. Significant interest and several applications have been reported for mono-disperse magnetic ferrite NPs in different research areas such as ferrofluids [1], imaging and therapy techniques [2], magnetic resonance imaging (MRI) [3], drug delivery and targeting [4]. Superparamagnetic behavior of metal oxide spinel ferrite NPs is a unique characteristic and highly particle size dependent. Many investigations showed that at the size range of below 30 nm which is known as single domain range [5–7], metal oxide NPs become superparamagnetic and can be used in biomedical applications [8].

In the cubic close-packed oxides of the crystal structure of ferrites, divalent and trivalent cations can occupy the octahedral and tetrahedral sites [9]. Different metal substitutions such as Zn^{2+}, Ni^{2+}, Mn^{2+}, Cr^{2+} and Cu^{2+} ions in the ferrite structures induce variations in the ferrite properties [10, 11]. For example, adding Ag NPs to $NiFe_2O_4$ induced changes in magnetic properties [12], or doping magnesia in nickel ferrite can give rise to an increase in the coercivity field (H_C), and at the same time complex dielectric permittivity of samples was decreased [13]. It was proved that adding cobalt to $MgFe_2O_4$ modifies the antibacterial activity of $MgFe_2O_4$ NPs [14]. The recent research showed that Ti and Cu doped nickel ferrite NPs demonstrated enhanced antibacterial activity [15]. In general, XFe_2O_4 NPs (X = Cu, Zn and Mn) are well-known inverse spinel ferrites with X^{2+} in B (octahedral) sites, where Fe^{3+} ions are divided equally among A (tetrahedral) and B (octahedral) sites [16]. Thereafter, XFe_2O_4 NPs (X = Cu, Zn and Mn) have attracted extensive attention due to their excellent phase stability, high magnetic permeability, high electrical conductivity, low eddy current loss, bandgap (~ 1.9 eV), low cost of production and non-toxicity [17]. So, by using diamagnetic and paramagnetic materials such as copper (Cu), zinc (Zn) and manganese (Mn), the structure of ferrite NPs could be modified to soft ferrite types. Soft magnetic materials display desired electrical, magnetic and optical properties, such as high value of resistivity, permeability, permittivity, saturation magnetization, low power losses and coercivity [18]. Therefore, above-mentioned features of this type of ferrites make them suitable for various applications [17, 19, 20]. These NPs can be used and are proposed for applications in the fields of drug delivery, magnetic hyperthermia, sensing, magnetic resonance imaging (MRI), antibacterial applications, photocatalytic activity and dentistry [21–27].

The research on substitution metal ferrite NPs have been mostly focused on their magnetic and structural characteristics [28–30]. Before implementation for biomedical applications, prepared NPs need optimization and some modification to increase and modify their biocompatibility and antibacterial activity. For example, infectious bacteria is the reason of dental caries, therefore it is important to control such diseases by using materials that have the killing or inactivation capability of the causative bacteria [25]. Also, the specific surface area in ferrite NPs is high which allows them to interact with the surface structures of bacteria. In addition, because they are fairly small in size, they can be uptaken by bacteria rapidly [31].

According to the chemical composition of an antibacterial agent, they can be categorized into two types: inorganic and organic agents. However, the disadvantages of organic antibacterial agents such as low heat resistance, high decomposability and short life expectancy cause limitation in their applications [32]. As a result, inorganic antibacterial agents have received more recognition in the antibacterial product market. Nano-inorganic metal oxides have potential to reduce bacterial contamination as they offer more advantages compared to organic compounds [25, 33]. On the other hand, magnetic NPs are effective in fighting infectious diseases as antibacterial agents which make them useful in wide range of applications such as food packaging and processing, textile industry, water and waste treatment and biomedical devices [34].

For example, bacterial microbes such as *Escherichia coli (E. coli), Staphylococcus aureus (S. aureus)* can be found in water and flood water, which are responsible for many skin diseases [35]. Recently, many research on spinel nanoparticles has been explored for their capability as photo catalyst in waste water treatment as well as for antibacterial activities to kill the bacteria strains which can cause infections of nail, skin and mucosal surfaces [35]. Hathout et al. showed that $CoFe_2O_4$ NPs are a promising candidate as antibacterial agent against different strains of bacteria and anticancer agent for food sector and medical applications [36]. For the ferrite preparation, different synthesis methods were shown, for instance Maaz et al. synthesized superparamagnetic nanoparticles of nickel ferrite by co-precipitation route and reported the value for the single-domain limit (~11 nm) that is in good agreement with calculated (theoretical) value for Ni-ferrite NPs [37]. Cabuil et al. reported the hydrothermal synthesis of cobalt ferrite ferrofluid based on NPs with an average diameter in the order of 11.9 and 18.7 nm by varying temperature and incubation time [37]. Nanocrystalline Ni–Zn-ferrite NPs were synthesized at room temperature by high-energy ball milling elsewhere [38]. Pillai et al. used water-in-oil micro-emulsion to prepare the NPs with a diameter of 50 nm after heat treatment [39]. Between different types of wet chemical methods, sol gel technique is well known for producing high purity, homogenous

powders with nano-meter dimension at comparatively low temperatures [40]. Sol–gel auto combustion is quite simple and low cost and has both chemical and physical processes [41], therefore sol–gel method is the preferred main option for preparation of advanced spinel ferrite materials [42–45].

To the best of our knowledge, there are limited number of reports and comparison studies between different types of ferrites, and the efficiency of prepared ferrite NPs with sol–gel method are high for antibacterial applications, notably with no cytotoxic effect on human body. Current study concentrates on sol–gel preparation of metal substitution on ferrite NPs (XFe_2O_4 with X = Cu, Zn and Mn). Structural properties, size distribution and surface morphology as well as magnetic and antibacterial properties of substituted ferrite NPs have been investigated. Gram negative (*E. coli*) and Gram positive (*S. aureus)* bacteria strains were used for demonstration of antibacterial activity. Cell viability and morphology were examined by methyl-thiazolyl-tetrazolium (MTT) cytotoxicity assay and phase contrast inverted microscopy. The outcome of this study will be helpful in finding new compounds with high antibacterial efficiency for using in different biomedical applications. The prepared inorganic compounds presented enhanced antibacterial activity in low concentration, further, some of them contain mineral elements which are essential to the human body [46–48].

Materials and Methods

Synthesis of Ferrite NPs

Metal nitrates; iron nitrate ($Fe(NO_3)_3{\cdot}9H_2O$), copper nitrate ($Cu(NO_3)_2{\cdot}6H_2O$), manganese nitrate ($Mn(NO_3)_2{\cdot}4H_2O$) and zinc nitrate ($Zn(NO_3)_2{\cdot}6H_2O$) of analytical grade were purchased from Merck, and used as precursors to prepare the $CuFe_2O_4$, $ZnFe_2O_4$ and $MnFe_2O_4$ NPs with the molar ratios of 2:1. Briefly, the metal nitrates were dissolved in distilled water to obtain a clear solution. Then, required concentrations of each solution were added to the other one in the desired molar ratio, and an aqueous solution of citric acid was added to the prepared solution. The pH of the solution was adjusted to 7, by drop wise addition of 25% aqueous ammonia [49]. Solution was heated at 80 °C for 3 h to transform it into gel, followed by a self-propagating combustion until the gels were completely burned out to form fluffy loosen powders. To remove any remaining water, prepared powder was placed in an oven at 180°C for overnight. To improve the crystallinity of the samples, prepared NPs were dried in an electrical vacuum furnace at 700 °C for 2 h [50].

Characterization of Ferrite NPs

The phase structure, elemental composition, particle size, morphology as well as magnetic properties of each synthesized powder were characterized by different methods including X-Ray Diffraction (XRD, Rigaku D/Max IIIC, Cu-Kα radiation), Transmission Electron Microscopy (TEM, JEOL JEM-1400), Field Emission Scanning Electron Microscopy with Energy Dispersive X-Ray Spectroscopy (FESEM-EDX, JEOL-instrument JSM-6490A), Fourier Transform Infrared Spectrometer (FT-IR, Model 783 Perkin Elmer Spectrometer) and Vibrating Sample Magnetometry (VSM, Lake Shore 7303–9309).

Determination of Antibacterial Activity

The antibacterial activities of synthesized ferrite NPs ($CuFe_2O_4$, $ZnFe_2O_4$ and $MnFe_2O_4$) were estimated by broth microdilution and Kirby-Bauer disk diffusion methods. Both Gram-positive (*S. aureus*) and Gram-negative (*E. coli*) bacteria were used as standard strains [51]. For evaluating the antibacterial activity of the NPs, all of the procedures were carried out according to the standards of the Clinical and Laboratory Standards Institute (CLSI) [52]. The total of 90 µL of serially diluted concentrations of synthesized $CuFe_2O_4$, $ZnFe_2O_4$ and $MnFe_2O_4$ NPs (from 1000 to 10 µg/ml) were added to each well of 96-well microtiter plates containing 10 µl of bacterial suspension (0.5 McFarland). Then, the microtiter plates were incubated at 3 °C for 24 h and subjected to evaluation of minimum inhibitory concentration (MIC) and minimum bactericidal concentration (MBC) [53]. Bacteria without nanoparticles were labelled as positive control. Later, the bacterial growth was measured by reading optical density at 600 nm by an ELISA microtiter plate reader (enzyme-linked immunosorbent assay). This procedure was performed in triplicates. Accordingly, the growth inhibition percentage (GI%) of the synthesized nanoparticles were calculated according to the following formula (Eq. 1) [54]:

$$\mathrm{GI\%} = \frac{\text{OD at the presence of NPs}}{\text{OD of positive control}} \times 100 \quad (1)$$

Kirby–Bauer Disc Diffusion Method

Sterile cotton swab was used for swabbing the bacterial suspension (10^6 CFU/ml) on the Muller Hinton Agar (MHA) plates. Then, impregnated paper discs by NPs were placed on the MHA plates and incubated for 24 h at 37 °C [55]. Moreover, the disc with antibiotic streptomycin (Himedia, 30 mg/disc) and a pieces of filter paper were used as positive

and negative controls, respectively. Later, the diameter of the zone of inhibition was measured and results were tabulated for evaluation of antibacterial activity by using Himedia zone scale [56]. To obtain the optimum results, all the experiments were carried out in triplicates.

The Cytotoxicity Effect

The MTT colorimetric assay was performed on human normal skin cell lines (HSF 1184) to evaluate the cytotoxicity of the synthesized nanoparticles [57]. In this technique, culture medium was studied as the negative control. The cells were maintained in advanced RPMI 1640 medium which contained 10% heat-inactivated fetal bovine serum (FBS) and 1% streptomycin-penicillin. Then, plates were incubated in a humidified atmosphere of 5% CO_2, 95% air at 37 °C. After that, 200 µl of cell suspension (5×10^4 cell/well) was placed in each well of a sterile 96-well microplate and incubated at 37 °C, 5% CO_2 and relative humidity of 98%. Then, 50 µl of different concentrations of $CuFe_2O_4$, $ZnFe_2O_4$ and $MnFe_2O_4$ NPs (0 to 1000 µg/ml) were replaced with previous media to the wells including cells. Next, 20 µl of MTT (thiazolyl blue tetrazolium bromide) dye (5 mg/ml in phosphate-buffered saline) was added to each well and incubated for 4 h. Afterward, to dissolve the formazan crystals formed in living cells, 200 µl of dimethyl sulfoxide (DMSO) solution was added to each well. Finally, after 15 min, the absorption of solution was recorded at a wavelength of 570 nm using an ELISA microtiter plate reader (enzyme-linked immunosorbent assay). This procedure was done in triplicates [58].

Results and Discussion

Physical Analysis

The XRD patterns of all the synthesized powders are shown in Fig. 1a. The peaks and the reflection planes are listed as follows: (2θ: 30.38°, 35.73°, 37.12°, 43.26°, 53.94°, 57.12° and 63.06°) and (220), (311), (222), (400), (422), (511) and (440). The diffraction peaks and their relative intensities are attributed to the cubic spinel structure, which confirms the synthesized powders with different compositions have monophasic nature [59]. In other words, the absence of any additional peaks associated to other second phases such as Fe_2O_3, CuO, ZnO, and MnO indicates the successful substitution of Cu, Zn, and Mn ions in the synthesized spinel structure of ferrite powders where fd3m space group is formed (JCPDS 008-0234) [59–61]. Additionally, the variation of the lattice parameter in a metal-substituted ferrite NPs supports the incorporation of metal ions into the host ferrite lattice [7].

The value of the lattice parameter is attributed to the difference in the ionic radii between Fe and other metals. The value of the lattice parameters and crystal size of each sample were calculated by the formula reported in Refs.

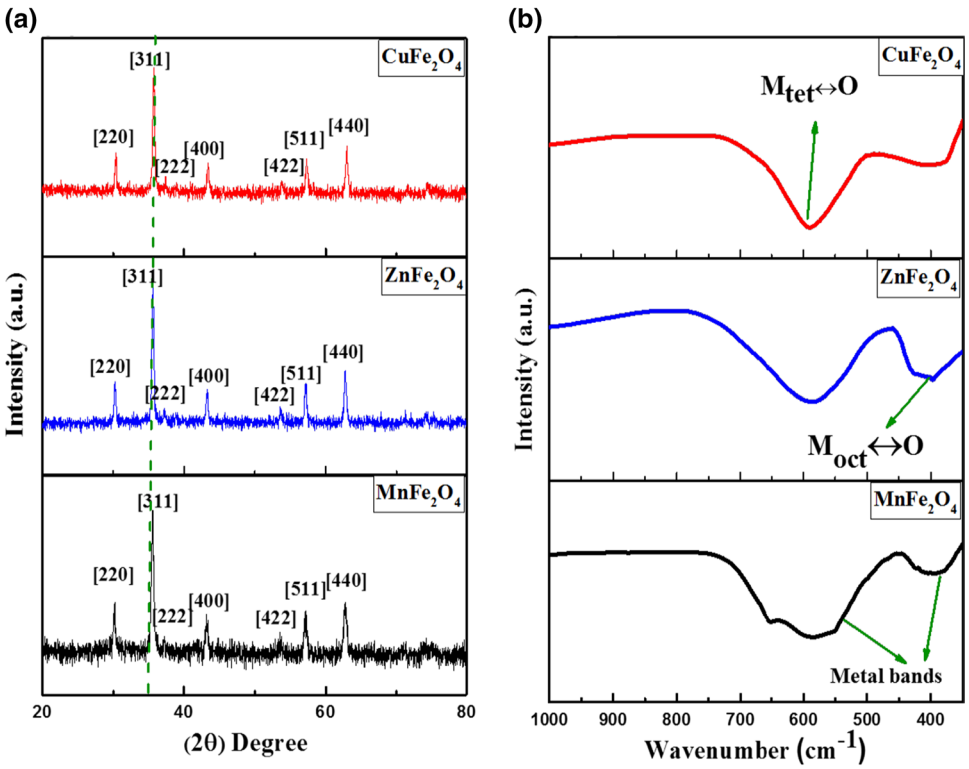

Fig. 1 **a** XRD spectra and **b** FT-IR patterns of $CuFe_2O_4$, $ZnFe_2O_4$ and $MnFe_2O_4$ NPs sintered at 700 °C

Table 1 Structural parameters calculated from X-ray diffraction studies for XFe_2O_4 (X = Cu, Zn, Mn)

XFe_2O_4 (X = Cu, Zn, Mn)	D_{XRD} (nm)	D_{FESEM} (nm)	Lattice constant (Å)
$CuFe_2O_4$	24.44	25–30	8.337 ± 0.08
$ZnFe_2O_4$	24.89	25–30	8.347 ± 0.08
$MnFe_2O_4$	24.98	25–30	8.361 ± 0.08

[7, 59, 62] and are provided in Table 1. $MnFe_2O_4$ powder had the largest lattice parameter in comparison with others which can be explained by the partial replacement of Fe ions by Mn, Zn, and Cu ions where the Mn ion has the largest ionic radius among others (Mn^{2+} = 0.91 Å, Zn^{2+} = 0.82 Å, Cu^{2+} = 0.73 Å and Fe^{2+} = 0.61 Å) [63–65]. The average crystalline size calculated via the Deby-Sherrer formula [64] was ~ 25 nm for each sample.

Room temperature Fourier-transform infrared (FTIR) spectroscopy in the range of 200–1000 cm^{-1} demonstrated the formation of metal substituted ferrite NPs (Fig. 1b) [62, 65]. Appearing band at the higher wave number (ν_1 = 585–595 cm^{-1}) is assigned to the tetrahedral complexes ($M_{tet} \leftrightarrow O$), while the band appearing at the lower wave number (ν_2 = 390–400 cm^{-1}) is assigned to the octahedral complexes ($M_{oct} \leftrightarrow O$). The octahedral cluster has a lower normal mode of vibration than the tetrahedral cluster [3]. It could be attributed to the shorter bond length of the tetrahedral cluster and longer bond length of the octahedral cluster [7]. FESEM micrographs of the synthesized $CuFe_2O_4$, $ZnFe_2O_4$, and $MnFe_2O_4$ NPs show nearly spherical shape for all (Fig. 2i) [7]. The corresponding particle size distribution for all powders indicates that the particle sizes were in the range of 20 to 30 nm (Fig. 2ii) [66]. The results of energy dispersive X-ray spectroscopy (EDX) analysis for all the samples are consistent with the expected results (i.e., the presence of Fe, Mn, Zn, Cu and O elements), and confirm the absence of impurities in the samples (Fig. 2iii) [7].

TEM was used to further characterize the size and morphology of the synthesized NPs, and it was confirmed that all NPs had smooth surfaces with well dispersed particles, and the size range of the NPs were between 20 to 30 nm (Fig. 3). Most particles appeared spherical in shape; however, some elongated particles were also present. Some moderately agglomerated particles as well as separated particles were observed in the samples. All the findings were in good agreement and consistent with the observations from XRD and FESEM images [62].

The room temperature magnetic hysteresis curves for prepared NPs were measured under an applied external field of up to 15 kOe and at a temperature of 300 K (Fig. 4) [62]. The *S* like shape of loops, which do not have coercivity, assigns the leading magnetic phase as superparamagnetic for all samples at room temperature [67]. Although $CuFe_2O_4$, $ZnFe_2O_4$ and $MnFe_2O_4$ are soft cubic ferrites, one can expect some magnitude of coercivity as reported elsewhere [68]. However, the observed superparamagnetic behavior revealed that the size range of synthesized particles (25–30 nm) is smaller than the critical size to observe a ferrimagnetic behavior [69]. Saturation magnetization (M_S) of each sample can be estimated by a method that is applied on hysteresis curves. Initially, M_S versus $1/H^2$ (H refers to applied magnetic field) graphs for the high magnetic field range of (10 kOe–15 kOe) were plotted. The linear fit to the plot intercepts the magnetization axis for zero magnitude of $1/H^2$ and gives an estimate value of M_S.

The estimated magnetic parameters *(Ms, Hc, Mr, and Mr/Ms)* belonging to all the samples are listed in Table 2 where the M_S values were found to be between 53 and 76 emu/g, and *Mr* (remnant magnetization) values were between 0.66 and 1.98 emu/g. These magnitudes are in good agreement with respect to reported data in the literature [70–72]. The S shape of the hysteresis loop for all samples with nanoparticle sizes less than 30 nm and small coercive fields in the present work *(Hc* ~ 0) prove the superparamagnetic behavior. The squareness ratio (*Mr/Ms*) in the present investigation remains below 0.50 which reveals that the synthesized materials are in multi magnetic domain. It has been reported in the literature that a squareness ratio below 0.5 can be attributed to the formation of a multi domain structure, in which domain wall movement allows for an easier change in orientation with applied field, And the squareness ratio at or above 0.5 indicates the material is around the single magnetic domain size.

The magnetic moment or magneton number (n_B) is another available magnetic parameter which could be evaluated by a well-known equation as given by (Eq. 2) [73]:

$$n_B = \frac{M_W \times M_S}{5585} \mu_B \tag{2}$$

where M_W is molecular weight and μ_B is Bohr magneton as unit of magneton number [73]. The magneton numbers for the synthesized $CuFe_2O_4$, $ZnFe_2O_4$ and $MnFe_2O_4$ NPs were determined as 2.45 μ_B, 2.29 μ_B and 3.12 μ_B, respectively. It was already mentioned that the average particle sizes were very close for all types of NPs. Hence, the main contribution to the net magnetic moment and saturation magnetization can be expected from individual magnetic moments of the divalent ions in the chemical formula where Mn^{2+} has 5 μ_B [74, 75] which has much higher moment than Cu^{2+} (2.64 μ_B) [53] and Zn^{2+} (0.68 μ_B) [76].

Antibacterial Properties

The antibacterial activity of nanoparticles against *S. aureus* and *E. coli* was studied using broth microdilution and disk diffusion methods. In the presence of NPs, growth of both

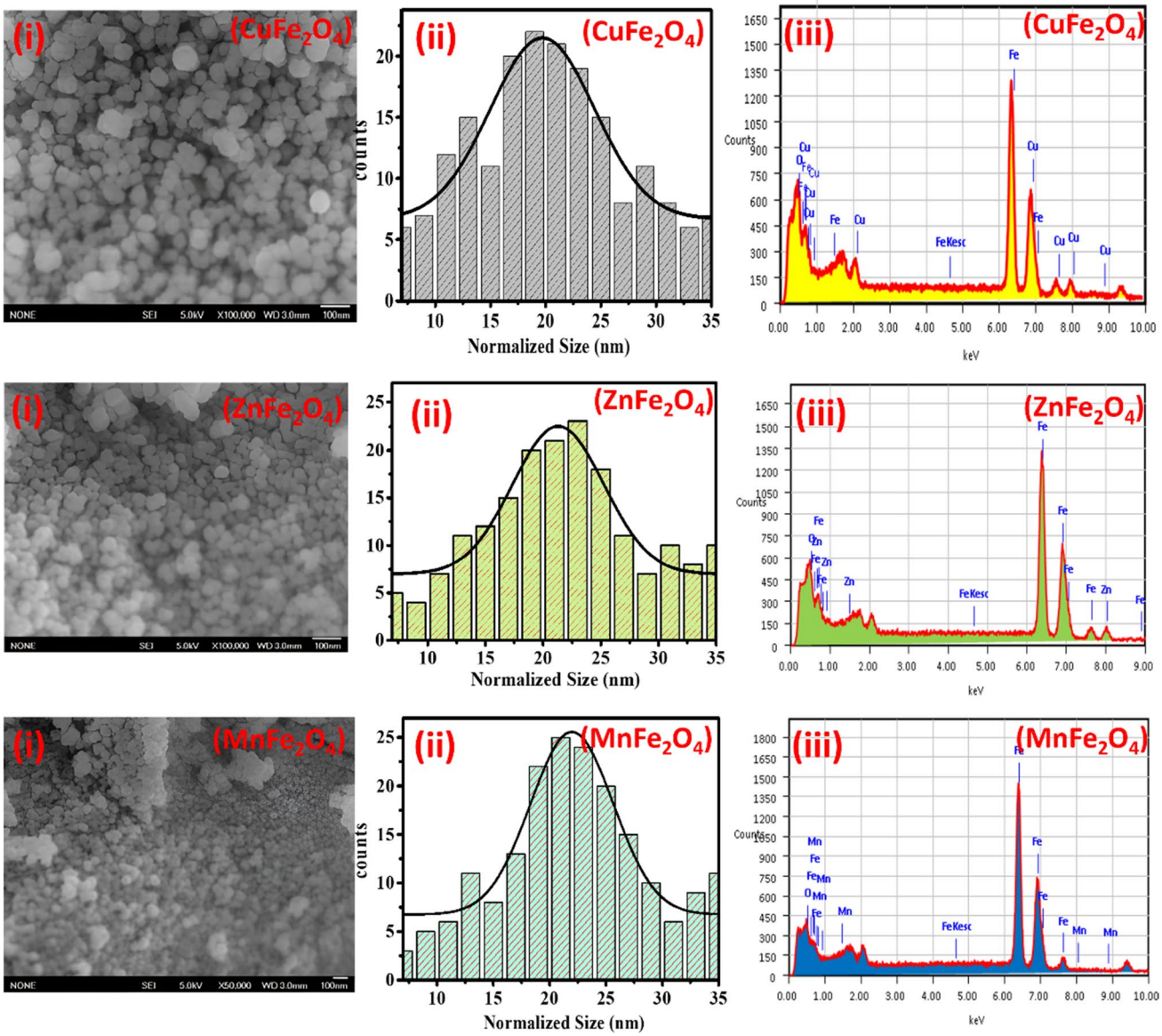

Fig. 2 **i** FESEM images, **ii** Particle size distribution histograms and **iii** EDX spectrograph of $CuFe_2O_4$, $ZnFe_2O_4$ and $MnFe_2O_4$ NPs

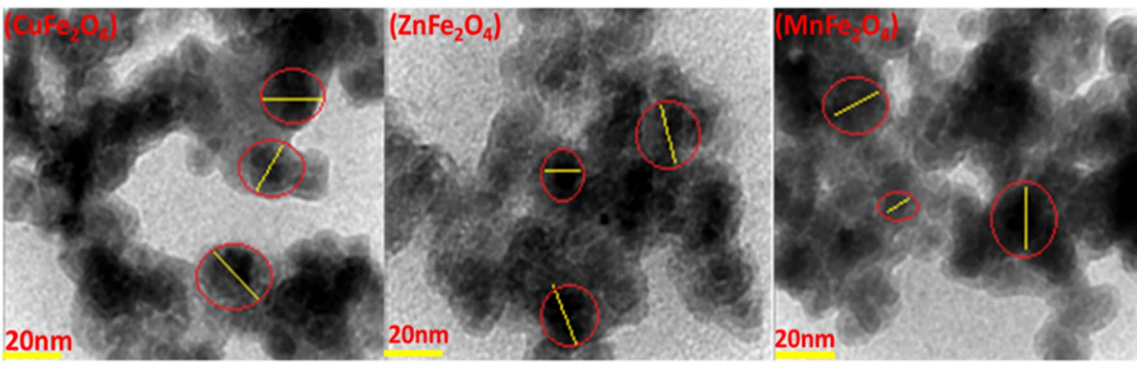

Fig. 3 Representative TEM images of $CuFe_2O_4$, $ZnFe_2O_4$ and $MnFe_2O_4$ NPs

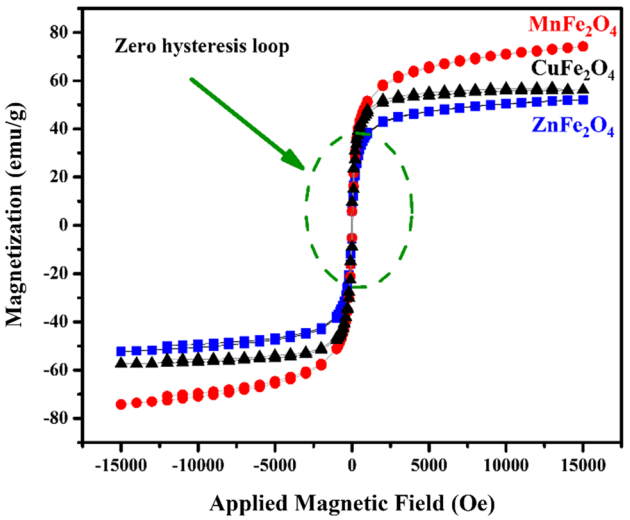

Fig. 4 The room temperature M–H curves of of $CuFe_2O_4$, $ZnFe_2O_4$ and $MnFe_2O_4$ NPs

Table 2 Magnetic parameters *(Ms, Hc, Mr, and Mr/Ms)* values for different ferrite nanoparticles

Sample	M_S (emu/g)	M_r (emu/g)	*Hc* (Oe)	*Mr/Ms*
$MnFe_2O_4$	67	0.66	~0	0.0098
$CuFe_2O_4$	53	1.33	~0	0.0250
$ZnFe_2O_4$	51	1.98	~0	0.388

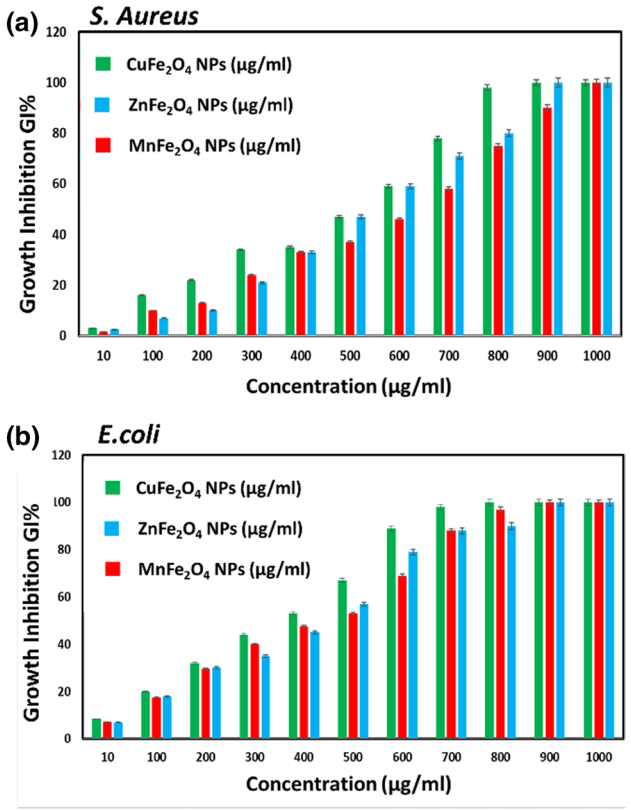

Fig. 5 Effect of different concentrations of $CuFe_2O_4$, $ZnFe_2O_4$ and $MnFe_2O_4$ NPs on growth inhibition of Gram-positive (*S. aureus*) and Gram-negative (*E. coli*) bacteria

bacteria was inhibited (Fig. 5). The bacterial growth inhibition gradually increased with increasing nanoparticle concentration. Moreover, $CuFe_2O_4$ NPs showed better antibacterial activity against *E. coli*. at a concentration of 400 µg/ml compared to other NPs. At this concentration, $CuFe_2O_4$, $MnFe_2O_4$ and $ZnFe_2O_4$ NPs displayed 53%, 47.5%, and 45% of bacterial growth inhibition, respectively. Several studies reported copper to have high contact kill rates on bacterial cells, including *E. coli*, similarly, bacterial cells exposed to copper were killed because they accumulated copper ions and exhibited membrane and cell envelope damage when in contact with the metallic copper ions [77]. The MIC and MBC values of nanoparticles are given in Table 3.

Among NPs, the lowest MIC (400 µg/ml) and MBC (800 µg/ml) values were obtained for $CuFe_2O_4$ NPs against *E. coli*. Besides, the highest value was achieved for $ZnFe_2O_4$ NPs against *S. aureus*. The results demonstrated stronger antibacterial activity of copper NPs than zinc NPs, that can be in correlation with a stronger affinity of Cu^{2+} for biomolecules. This observation is in agreement with previous reports that compares antibacterial activity of various metals (copper and zinc) [78].

The viability of the bacteria was assessed by determining the clear zone of inhibition around the samples after 24 h incubation. The obtained results are provided in Table 4, and the corresponding images of inhibition zones and the schematic diagrams of the antibacterial activity of the prepared NPs are shown in Fig. 6.

The disc diffusion results confirmed the MIC and MBC results. Higher antibacterial activity was observed at presence of $CuFe_2O_4$, $ZnFe_2O_4$ and $MnFe_2O_4$ NPs against the *E. coli* with inhibition zones of 22, 20 and 19 mm, respectively, compared to Fe_2O_4 that almost had no effect on both types of bacteria strains. The recorded antibacterial activity of the NPs is higher than that of the standard streptomycin which is the commonly used commercial antibacterial control agent. Obtaining an inhibition zone with a diameter of 22 mm indicates a good antibacterial activity against the investigated bacteria [79]. Besides, the growth of *S. aureus* was inhibited by $CuFe_2O_4$ NPs with a maximum inhibition zone of 18 mm. Similar antibacterial effect of NPs was reported elsewhere [79, 80].

Hashim et al. reported that the nanosized particles greatly influence the antibacterial activity, against various microorganisms [81]. The efficient antibacterial property of their prepared ferrite NPs was due to large surface area, which provided better contact with the microorganisms, and the

Table 3 Minimum inhibitory concentration (MIC) and minimum bactericidal concentration (MBC) data of the NPs (in µg/ml) for Gram-negative and Gram-positive bacteria

Bacterial strains	$CuFe_2O_4$ NPs (µg/ml)		$ZnFe_2O_4$ NPs (µg/ml)		$MnFe_2O_4$ NPs (µg/ml)	
	MIC	MBC	MIC	MBC	MIC	MBC
S. aureus	600	900	700	1000	600	900
E. coli	400	800	500	900	500	900

Table 4 The antibacterial activity of ferrite and (Zn, Cu, and Mn) ferrite NPs against some pathogenic bacteria

Bacterial strains	Zone of inhibition (mm)			
	Fe_2O_4	$MnFe_2O_4$	$ZnFe_2O_4$	$CuFe_2O_4$
E. coli	3.7	19	20	22
S. aureus	~0	12.4	17	18

antibacterial activity of metal oxide NPs was caused by generation of reactive oxygen species (ROS) and release of toxic metals from the core of NPs.

The bactericidal effect of NPs may be due to their small size, as Mehrabi et al. reported that decrease in the size of NPs and increase in surface to volume ratio increase the antibacterial activity of the nanomaterials [80]. According to Alsafari et al. [82], the inactivation of *E. coli* by zero-valent iron NPs could be due to the penetration of the small particles (10–80 nm) into *E. coli* membranes, which causes oxidative stress and cell membrane disruption. The bactericidal mechanism of NPs is not fully elucidated, yet studies have advised that when *E. coli* was treated with NPs, changes in bacterial membrane morphology were reported [83]. As a consequence of present functional groups such as carboxyl, hydroxyl and phosphate on the surface of bacterial cell walls, the overall charge of bacteria at biological pH value is negative. The electrostatic interaction between (Cu^{2+}, Zn^{2+} and Mn^{2+}) ions and the functional groups of negatively charged cell membrane facilitates attachment of ions onto cell membranes and causes the inhibition of respiratory chain enzymes and eventually cell death [84]. Gram-negative bacteria contains lipopolysaccharides (LPS) in the cell membrane, besides there is only a thin peptidoglycan layer between the cytoplasmic membrane and the outer membrane of their cell wall. These differences in structure, thickness and composition of cell can explain why Gram-negative *E. coli* shows substantial inhibition [85]. Typical FESEM images indicate the morphology of the *E. coli* bacteria attached to the glass surface as well as the metal-substituted ferrite NPs (Fig. 7). The compared antibacterial activity of NPs on micro-organisms based on FESEM micrographs is found as $CuFe_2O_4 > ZnFe_2O_4 > MnFe_2O_4$.

The highest antibacterial activity was observed for copper substituted ferrite NPs, as copper results in significant growth inhibition of bacteria [7, 63]. It was reported that when $CuFe_2O_4$ NPs interact with an aqueous phase, Cu^{2+} ions are released [82]. The antibacterial mechanism of Cu^{2+} ions has been attributed to the fact that ions are absorbed by

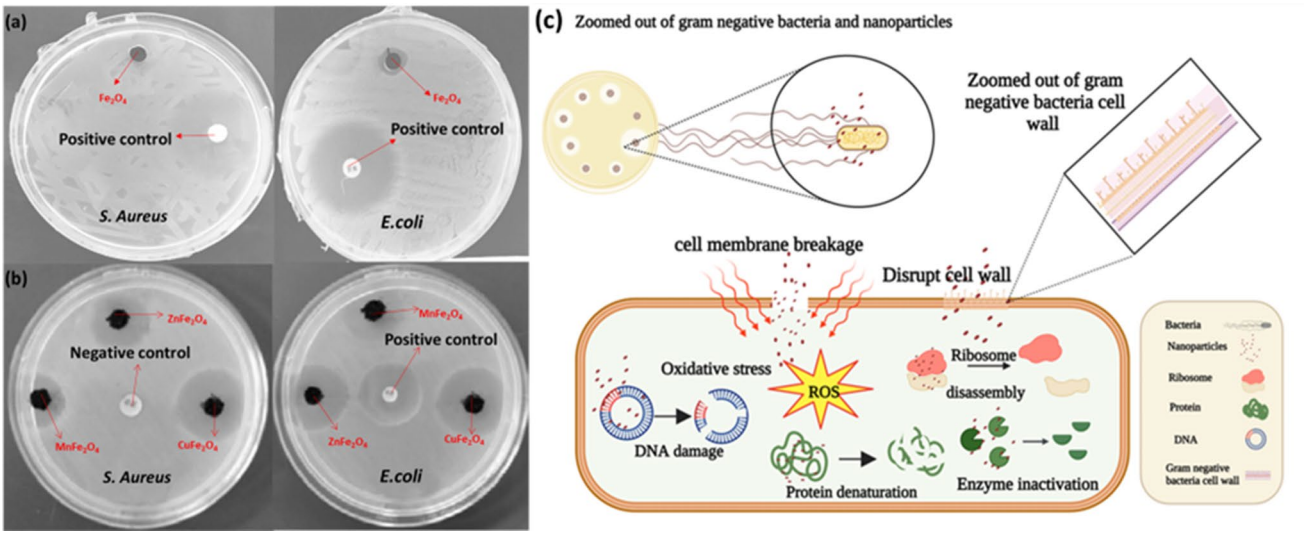

Fig. 6 **a** Zone of inhibition produced by Fe_2O_4, **b** $CuFe_2O_4$, $ZnFe_2O_4$ and $MnFe_2O_4$ NPs against both Gram-positive and Gram-negative bacterial strains. **c** Schematic diagram of antibacterial activity mechanism of the nanoparticles

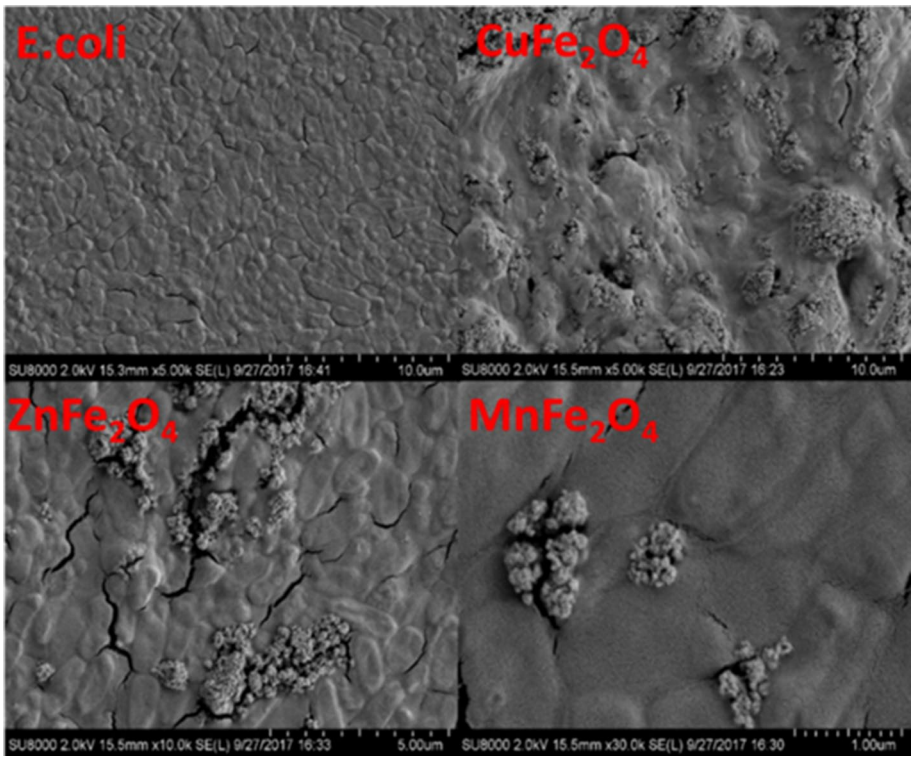

Fig. 7 FESEM images of the untreated *E. coli* bacteria and treated with $CuFe_2O_4$, $ZnFe_2O_4$, and $MnFe_2O_4$ NPs at MIC values (50% of bacterial growth was inhibited), where morphological deformities can be seen

bacteria at higher concentrations. Copper ions are absorbed onto the bacterial cell surface, imparting damage to the cell membrane by solidifying protein structure or altering enzyme function. The mechanism of the antibacterial action of Cu^{2+} ions involve the binding of Cu^{2+} ions to the functional groups of proteins and enzymes, which causes inactivation and inhibition in cellular processes of bacteria. Copper ions have the ability to kill bacteria by generating reactive oxygen species (ROS) and destroying their cell walls and membranes. ROS can cause damage to proteins and DNA of bacteria [83].

The Cytotoxicity Effect

The MTT colorimetric assay was performed on human normal skin cell lines (HSF 1184) to evaluate the cytotoxic potential of the synthesized NPs. The percentage of cell viability in the presence of different concentrations of $CuFe_2O_4$, $ZnFe_2O_4$ and $MnFe_2O_4$ NPs was investigated. The results revealed that up to the tested concentrations of 400 µg/ml of NPs, no major difference in terms of cellular viability was detected in comparison with the control cells and percentage viability was in the range 98 to 100% (Fig. 8a). However, the higher cytotoxicity toward HSF 1184 cells was achieved for $CuFe_2O_4$ NPs compared to other NPs. More than 60% of cell growth was prevented at a concentration of 1000 µg/ml for $CuFe_2O_4$ NPs, whereas only 59% and 43% of cell growth inhibition at the same concentration was observed for $MnFe_2O_4$ and $ZnFe_2O_4$ NPs, respectively. The higher cytotoxic effect of copper is due to its being a transition metal that increases the generation of reactive oxygen species (ROS) which may disturb the integrity of the cell membrane [86, 87]. The results of the percentage viability of HSF 1184 cells indicated that increasing the concentration of NPs led to dose-dependent rise in mitochondrial dysfunction. Mechanism of cytotoxicity can be explained by ions (Cu^{2+}, Zn^{2+} and Mn^{2+}) of NPs entering into cells and leading to mitochondrial dysfunction, protein and DNA damage and finally apoptosis and inhibition of cell proliferation [88]. In order to study the morphological changes in the HSF 1184 cells after treatment with various concentrations of different NPs, an inverted microscope was used (Fig. 8b). The morphological changes such as rounding of cells, detachment and cell lysis were clearly observed after treatment of cells at a concentration of 1000 µg/ml. Similar to the present findings, studies were also conducted by others to investigate the cytotoxic activity of nanoparticles, but unlike other NPs, $CuFe_2O_4$ NPs had less toxicity on human cell lines while they had high toxicity effect on bacterial cells [88].

Conclusions

Metal-substituted ferrite NPs with sizes less than 30 nm were prepared by using sol–gel method, and their cubic spinel structure was confirmed by XRD. Although

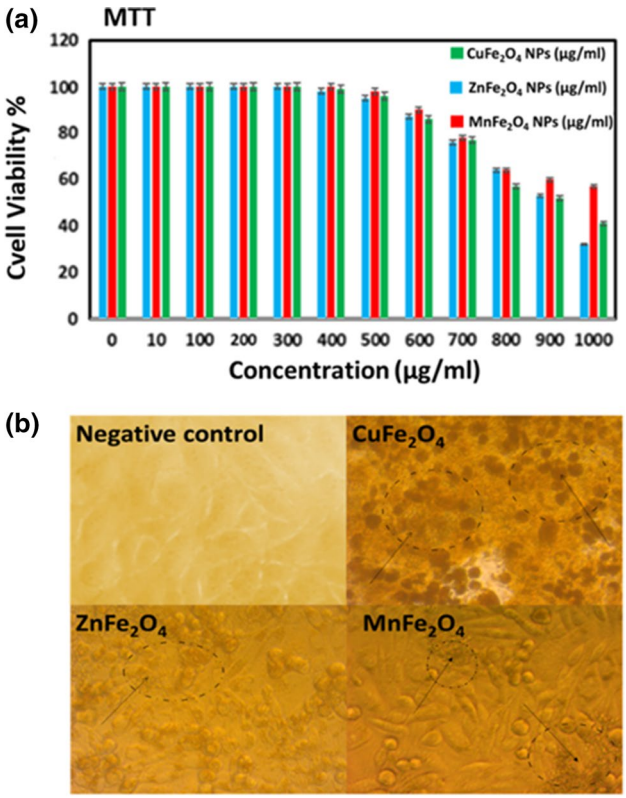

Fig. 8 **a** The percentage of cell viability of HSF 1184 cells in the presence of different concentrations of $CuFe_2O_4$, $ZnFe_2O_4$, and $MnFe_2O_4$ NPs. **b** Inverted microscope images of HSF 1184 normal cells as negative control, and HSF 1184 after treatment by $CuFe_2O_4$, $ZnFe_2O_4$, and $MnFe_2O_4$ NPs, showing cytotoxic effects which was determined by MTT assay

some elongated NPs were observed, they were mostly in spherical shape. Magnetic hysteresis loops revealed the superparamagnetic nature of all synthesized NPs at room temperature which is desired in biomedical applications. $MnFe_2O_4$ NPs had almost 50% higher M_S and n_B compared to $CuFe_2O_4$ and $ZnFe_2O_4$ NPs. Antibacterial activity against *E. coli* and *S. aureus* was significantly improved by metal (zinc, copper, and manganese) substitution, and copper spinel ferrite NPs showed the highest antibacterial activity among all prepared NPs. Transition metal-substituted ferrite NPs had greater antibacterial activity against *E. coli* than against *S. aureus*. The antibacterial functionality is associated with various mechanisms, including damaging the bacterial DNA, altering protein synthesis and membrane integrity. Our findings showed that zinc, copper, manganese ferrite NPs can be used in drug delivery systems and other biomedical applications due to their high biocompatibility and antibacterial activity.

Funding This research was supported by 2232 International Fellowship for Outstanding Researchers Program of TÜBİTAK (Project No: 118C346).

Data Availability The authors confirm the absence of sharing data.

Declarations

Conflicts of Interest The authors declare that they have no known competing financial interests or personal relationships that could have appeared to influence the work reported in this paper.

References

1. A. Amirabadizadeh, Z. Salighe, R. Sarhaddi, and Z. Lotfollahi (2017). *Journal of Magnetism and Magnetic Materials* **434**, 78. https://doi.org/10.1016/j.jmmm.2017.03.023.
2. I. Sharifi, H. Shokrollahi, and S. Amiri (2012). *Journal of Magnetism and Magnetic Materials* **324**, 903. https://doi.org/10.1016/j.jmmm.2011.10.017.
3. H. Yang, C. Zhang, X. Shi, et al. (2010). *Biomaterials* **31**, 3667. https://doi.org/10.1016/j.biomaterials.2010.01.055.
4. H. Wu, G. Liu, X. Wang, et al. (2011). *Acta Biomaterialia* **7**, 3496. https://doi.org/10.1016/j.actbio.2011.05.031.
5. A. A. Ati, Z. Othaman, and A. Samavati (2013). *Journal of Molecular Structure* **1052**, 177. https://doi.org/10.1016/j.molstruc.2013.08.040.
6. K. Mandal, S. Chakraverty, S. Pan Mandal, P. Agudo, M. Pal, and D. Chakravorty (2002). *Journal of applied physics* **92**, 501.
7. S. Dabagh, A. A. Ati, R. M. Rosnan, S. Zare, and Z. Othaman (2015). *Materials Science in Semiconductor Processing* **33**, 1. https://doi.org/10.1016/j.mssp.2015.01.025.
8. M. Irfan Hussain, M. Xia, K. Akhtar, A. Nawaz, S. Sharma, and Y. Javed, *Magnetic nanoheterostructures* (Springer, 2020).
9. K. E. Sickafus, J. M. Wills, and N. W. Grimes (1999). *Journal of the American Ceramic Society* **82**, 3279.
10. H. Deligöz, A. Baykal, E. Tanrıverdi, Z. Durmus, and M. S. Toprak (2012). *Materials Research Bulletin* **47**, 537.
11. M. Zahraei, A. Monshi, M. del Puerto Morales, D. Shahbazi-Gahrouei, M. Amirnasr, and B. Behdadfar (2015). *Journal of Magnetism and Magnetic Materials* **393**, 429. https://doi.org/10.1016/j.jmmm.2015.06.006.
12. A. Hao, M. Ismail, S. He, et al. (2017). *RSC Advances* **7**, 46665.
13. H. Moradmard, S. FarjamiShayesteh, P. Tohidi, Z. Abbas, and M. Khaleghi (2015). *Journal of Alloys and Compounds* **650**, 116. https://doi.org/10.1016/j.jallcom.2015.07.269.
14. C. Ehi-Eromosele, J. Olugbuyirozz, O. Taiwo, O. Bamgboye, and C. Ango (2018). *Bulletin of the Chemical Society of Ethiopia* **32**, 451.
15. G. N. Rajivgandhi, G. Ramachandran, C. C. Kanisha, et al. (2021). *Results in Physics* **23**, 104065. https://doi.org/10.1016/j.rinp.2021.104065.
16. Z. Szotek, W. Temmerman, D. Ködderitzsch, A. Svane, L. Petit, and H. Winter (2006). *Physical Review B* **74**, 174431.
17. T. Dippong, E. A. Levei, and O. Cadar (2021). *Nanomaterials* **11**, 1560.
18. Y. Ertas and L.-S. Bouchard (2017). *Journal of Applied Physics* **121**, 093902.
19. P. Thakur, D. Chahar, S. Taneja, N. Bhalla, and A. Thakur (2020). *Ceramics International* **46**, 15740. https://doi.org/10.1016/j.ceramint.2020.03.287.
20. H. Shokrollahi (2013). *Materials Science and Engineering: C* **33**, 2476.

21. M. Amiri, M. Salavati-Niasari, and A. Akbari (2019). *Advances in Colloid and Interface Science* **265**, 29.
22. S. Nasrin, F.-U.-Z. Chowdhury, and S. Hoque (2019). *Journal of Magnetism and Magnetic Materials* **479**, 126.
23. M. A. Maksoud, G. S. El-Sayyad, A. Ashour, et al. (2019). *Microbial pathogenesis* **127**, 144.
24. Y. Xu, Q. Liu, M. Xie, et al. (2018). *Journal of Colloid and Interface Science* **528**, 70. https://doi.org/10.1016/j.jcis.2018.05.066.
25. M. Fang, J.-H. Chen, X.-L. Xu, P.-H. Yang, and H. F. Hildebrand (2006). *International Journal of Antimicrobial Agents* **27**, 513.
26. H Nosrati, M Salehiabar, F Mozafari, et al. (2022) Applied Organometallic Chemistry: e6861.
27. A Bigham, V Rahimkhoei, P Abasian, et al. (2021) Chemical Engineering Journal: 134146.
28. S. Mallesh and V. Srinivas (2019). *Journal of Magnetism and Magnetic Materials* **475**, 290.
29. A. V. Malyshev, A. B. Petrova, A. P. Surzhikov, and A. N. Sokolovskiy (2019). *Ceramics International* **45**, 2719. https://doi.org/10.1016/j.ceramint.2018.09.114.
30. X. Zhou, Y. Zhou, L. Zhou, J. Wei, J. Wu, and D. Yao (2019). *Ceramics International* **45**, 6236. https://doi.org/10.1016/j.ceramint.2018.12.102.
31. M. A. Ansari, A. Baykal, S. Asiri, and S. Rehman (2018). *Journal of Inorganic and Organometallic Polymers and Materials* **28**, 2316.
32. Z.-X. Tang and B.-F. Lv (2014). *Brazilian Journal of Chemical Engineering* **31**, 591.
33. I. L. Liakos, M. H. Abdellatif, C. Innocenti, et al. (2016). *Molecules* **21**, 520.
34. J. V. Pande, A. B. Bindwal, Y. B. Pakade, and R. B. Biniwale (2018). *International Journal of Hydrogen Energy* **43**, 7411. https://doi.org/10.1016/j.ijhydene.2018.02.105.
35. M. K. Satheeshkumar, E. R. Kumar, C. Srinivas, et al. (2019). *Journal of Magnetism and Magnetic Materials* **469**, 691. https://doi.org/10.1016/j.jmmm.2018.09.039.
36. A. S. Hathout, A. Aljawish, B. A. Sabry, et al. (2017). *Journal of Applied Pharmaceutical Science* **7**, 086.
37. K. Maaz, S. Karim, A. Mumtaz, S. K. Hasanain, J. Liu, and J. L. Duan (2009). *Journal of Magnetism and Magnetic Materials* **321**, 1838. https://doi.org/10.1016/j.jmmm.2008.11.098.
38. S. Bid and S. K. Pradhan (2004). *Materials Chemistry and Physics* **84**, 291. https://doi.org/10.1016/j.matchemphys.2003.08.012.
39. V. Pillai and D. O. Shah (1996). *Journal of Magnetism and Magnetic Materials* **163**, 243. https://doi.org/10.1016/S0304-8853(96)00280-6.
40. D. Navas, S. Fuentes, A. Castro-Alvarez, and E. Chavez-Angel (2021). *Gels* **7**, 275.
41. S. T. Aruna and A. S. Mukasyan (2008). *Current Opinion in Solid State and Materials Science* **12**, 44. https://doi.org/10.1016/j.cossms.2008.12.002.
42. L. Guo, X. Shen, X. Meng, and Y. Feng (2010). *Journal of Alloys and Compounds* **490**, 301. https://doi.org/10.1016/j.jallcom.2009.09.182.
43. J. Azadmanjiri (2008). *Materials Chemistry and Physics* **109**, 109. https://doi.org/10.1016/j.matchemphys.2007.11.001.
44. R. S. de Biasi, A. B. S. Figueiredo, A. A. R. Fernandes, and C. Larica (2007). *Solid State Communications* **144**, 15. https://doi.org/10.1016/j.ssc.2007.07.031.
45. A. V. Raut, R. S. Barkule, D. R. Shengule, and K. M. Jadhav (2014). *Journal of Magnetism and Magnetic Materials* **358–359**, 87. https://doi.org/10.1016/j.jmmm.2014.01.039.
46. H. H. Sandstead (1994). *The Journal of Laboratory and Clinical Medicine* **124**, 322.
47. Y. Nishito and T. Kambe (2018). *Journal of Nutritional Science and Vitaminology* **64**, 1.
48. M. Roselli, A. Finamore, I. Garaguso, M. S. Britti, and E. Mengheri (2003). *The Journal of Nutrition* **133**, 4077.
49. A. Sutka and G. Mezinskis (2012). *Frontiers of Materials Science* **6**, 128.
50. Y. N. Ertas, N. N. Jarenwattananon, and L.-S. Bouchard (2015). *Chemistry of Materials* **27**, 5371.
51. Z. Ni, X. Gu, Y. He, et al. (2018). *RSC Advances* **8**, 41722.
52. S. M. Mousavi, S. A. Hashemi, Y. Ghasemi, et al. (2018). *Artificial Cells, Nanomedicine, and Biotechnology* **46**, S855.
53. R. Heydari, M. F. Koudehi, and S. M. Pourmortazavi (2019). *ChemistrySelect* **4**, 531.
54. B. A. Edhari, M. Mashreghi, A. Makhdoumi, and M. Darroudi (2021). *Journal of Trace Elements in Medicine and Biology* **68**, 126840. https://doi.org/10.1016/j.jtemb.2021.126840.
55. S. Jabbar Shawkat and K. Chehri (2021). *Avicenna J Clin Microbiol Infect* **8**, 123. https://doi.org/10.34172/ajcmi.2021.23.
56. D. O. Morais, A. Pancotti, G. S. de Souza, et al. (2021). *Journal of Materials Science: Materials in Medicine* **32**, 1.
57. S. Muzammil, M. Khurshid, I. Nawaz, et al. (2020). *Biofouling* **36**, 492. https://doi.org/10.1080/08927014.2020.1776856.
58. M. Amooei, Z. Meshkati, R. Nasiri, and A. B. Dakhili (2021). *Ecotoxicology and Environmental Safety* **209**, 111785. https://doi.org/10.1016/j.ecoenv.2020.111785.
59. M. G. Naseri, E. B. Saion, M. Hashim, A. H. Shaari, and H. A. Ahangar (2011). *Solid State Communications* **151**, 1031. https://doi.org/10.1016/j.ssc.2011.04.018.
60. M. Houshiar and L. Jamilpanah (2018). *Materials Research Bulletin* **98**, 213.
61. S. Sultana, Rafiuddin, M. Zain Khan, and K. Umar (2012). *Journal of Alloys and Compounds* **535**, 44. https://doi.org/10.1016/j.jallcom.2012.04.081.
62. S. Dabagh, K. Chaudhary, Z. Haider, and J. Ali (2018). *Results in Physics* **8**, 93.
63. S. Goh, C. Chia, S. Zakaria, et al. (2010). *Materials Chemistry and Physics* **120**, 31.
64. M. N. Ashiq, M. J. Iqbal, M. Najam-ul-Haq, P. H. Gomez, and A. M. Qureshi (2012). *Journal of Magnetism and Magnetic Materials* **324**, 15.
65. C. Cannas, A. Falqui, A. Musinu, D. Peddis, and G. Piccaluga (2006). *Journal of Nanoparticle Research* **8**, 255.
66. J. H. Almaki, R. Nasiri, A. Idris, et al. (2016). *Nanotechnology* **27**, 105601.
67. M. A. Almessiere, Y. Slimani, A. D. Korkmaz, et al. (2019). *Ultrasonics Sonochemistry* **54**, 1. https://doi.org/10.1016/j.ultsonch.2019.02.022.
68. A. Hajalilou and S. A. Mazlan (2016). *Applied Physics A* **122**, 1.
69. S. Mallesh, V. Srinivas, M. Vasundhara, and K. H. Kim (2020). *Physica B: Condensed Matter* **582**, 411963. https://doi.org/10.1016/j.physb.2019.411963.
70. Y. Behra and N. Singh (2018). *Materials Today: Proceedings* **5**, 15451.
71. G. Goya, H. Rechenberg, and J. Jiang (1998). *Journal of applied physics* **84**, 1101.
72. C.-R. Lin, Y.-M. Chu, and S.-C. Wang (2006). *Materials Letters* **60**, 447.
73. M Satalkar, N Ghodke, S Kane (2014) Journal of Physics: Conference Series. IOP Publishing.
74. S. Faraji, G. Dini, and M. Zahraei (2019). *Journal of Magnetism and Magnetic Materials* **475**, 137.
75. M. Almessiere, Y. Slimani, A. D. Korkmaz, et al. (2020). *Ultrasonics Sonochemistry* **61**, 104836.
76. Z. Huang, Q. Chen, S. Jiang, S. Dong, and Y. Zhai (2018). *AIP Advances* **8**, 055807.
77. I. D. Akhidime, F. Saubade, P. S. Benson, et al. (2019). *Food and Bioproducts Processing* **113**, 68. https://doi.org/10.1016/j.fbp.2018.09.003.

78. A. Varkey (2010). *Scientific Research and Essays* **5**, 3834.
79. S. Ayazi, M. Ghorbani, and R. Abedini (2021). *Chemical Engineering Research and Design* **169**, 214.
80. S. Rajabi and S. Sohrabnezhad (2018). *Journal of Fluorine Chemistry* **206**, 36.
81. M. Hashim, S. E. Shirsath, S. Meena, et al. (2013). *Journal of Magnetism and Magnetic Materials* **341**, 148.
82. I. A. Alsafari, S. Munir, S. Zulfiqar, M. S. Saif, M. F. Warsi, and M. Shahid (2021). *Ceramics International* **47**, 28874.
83. L. Gabrielyan, H. Badalyan, V. Gevorgyan, and A. Trchounian (2020). *Scientific Reports* **10**, 1.
84. N. MahmoudiKhatir, Z. Abdul-Malek, A. K. Zak, A. Akbari, and F. Sabbagh (2016). *Journal of Sol-Gel Science and Technology* **78**, 91.
85. M. Esfahanian, M. A. Ghasemzadeh, and S. M. H. Razavian (2019). *Artificial Cells, Nanomedicine, and Biotechnology* **47**, 2024.
86. S. S. Mondal, N. Jaiswal, P. S. Bera, et al. (2021). *Applied Organometallic Chemistry* **35**, e6026.
87. Y. Jiang, Z. Huo, X. Qi, T. Zuo, and Z. Wu (2022). *Nanomedicine* **17**, 303.
88. Z. Lin, Y. Li, G. Gong, et al. (2018). *International Journal of Nanomedicine* **13**, 5787.

Authors and Affiliations

Shadab Dabagh[1] · Somayeh Asadi Haris[2] · Yavuz Nuri Ertas[1,3]

[1] ERNAM—Nanotechnology Research and Application Center, Erciyes University, Kayseri 38039, Turkey

[2] Department of Cellular and Molecular Biology, Shahid Beheshti University, Tehran, Iran

[3] Department of Biomedical Engineering, Erciyes University, Kayseri 38039, Turkey